Aerospace Science and Technology 172 (2026) 111682

Contents lists available at ScienceDirect

Aerospace Science and Technology

journal homepage: www.elsevier.com/locate/aescte

Radar characterization of hypersonic wake plasma in a high-enthalpy shock-tunnel flow: RCS, micro-doppler and electron-density analysis

René Petervari [a,*], Sebastian Karl [b], Alexander Wagner [b], Peter Knott [a,c]

[a] Fraunhofer Institute for High Frequency Physics and Radar Techniques FHR, Fraunhoferstraße 20, Wachtberg, 53343, Germany
[b] Institute for Aerodynamics and Flow Technology, German Aerospace Center (DLR), Bunsenstraße 10, Göttingen, 35053, Germany
[c] Radar Systems Engineering, Institute of High Frequency Technology (IHF), RWTH Aachen University, Melatener Str. 25, Aachen, 52056, Germany

ARTICLE INFO

Communicated by Cummings Russell

Keywords:
Plasma sheaths
Radar signature
Aerospace simulation
Radar measurements
Wind tunnels
CFD
CEM

ABSTRACT

The plasma sheath that forms around vehicles at hypersonic speed can change the radar signature substantially. A common approach to predict the impact of plasma on radar observation is to combine computational fluid dynamics (CFD) and computational electromagnetics (CEM). Due to the lack of experimental reference data, however, these predictions often remain unvalidated and their accuracy unclear. As part of an initiative to improve this situation, this paper presents radar signatures of a turbulent flow around an 8 cm diameter sphere measured at high enthalpy conditions in the High Enthalpy Shock Tunnel Göttingen (HEG) at the site of the German Aerospace Center (DLR) in Göttingen. The radar return and microwave transmission of this instationary and turbulent hypersonic flow were acquired with the wideband Multi-application Software Defined Radar (Masodera) system. Besides a strong radio blackout on the transmission channel, characteristic Micro-Doppler features were also observed. Reference CFD and CEM simulations were carried out and are compared with the measured data.

1. Introduction

The development of new highly maneuverable hypersonic weapons poses a serious threat to today's air defense infrastructures. Radar systems are a central component of these and as such they must be enabled to reliably handle these new targets. Besides their tremendous speed that challenges traditional signal processing schemes [1], the generation of plasma at high Mach numbers can change radar signatures significantly [2,3] and thus affect critical system parameters like detection range, track stability or classification rates. All of these are vital for a successful intercept. Potential interference caused by plasma should be included and mitigated if possible. Furthermore, the uncertainty generally leads to larger margins in the system design and hence more expensive and less effective solutions. This is especially true for hypersonics and hypersonic defense.

A major reason for this uncertainty is the lack of reference data to validate the numerical models for hypersonic targets. To show this, we consider the underlying physical processes first. At hypersonic speed, the plasma sheath around a vehicle is generated by chemical reactions in high temperature air. Typically, high temperature regions emerge in stagnation and compression zones and inside the boundary layer (see e.g. [4]). The generated plasma is then transported along the stream lines. Typical air defense radar systems operate at microwave frequencies in the MHz and GHz range and with respect to microwaves, plasma can be modelled as a lossy, dielectric medium [5, p.136]. Its dielectric properties are predominantly determined by the local density of electrons and the rate of collisions with heavy particles (collision frequency). The former determines the cut-off frequency (plasma frequency) which limits the propagation of electromagnetic waves inside plasma and makes it opaque and reflective, while the latter inhibits the motion of the electrons which causes absorption and at high collision rates diminishes all plasma effects and thus restores wave propagation within the cut-off area. Hence, to determine the electromagnetic properties and to simulate respective signatures using CEM, detailed knowledge of microscopic quantities in the flow field like electron, atomic and molecular number densities is required. Today, the only way to obtain this information is CFD simulation. Given the limited experimental validation in high temperature, hypersonic flows, however, it is rather uncertain how accurate these predictions are. In the RAM C-II flight test case [6] - one of the few test cases available - different solvers produce discrepancies in the order of a magnitude while the precision of the measured data does not allow favoring any of the solutions [3,7]. Each solver incorporates various models with varying confidence to respect the multitude of physical effects involved. A good overview is given in Karl and Bykerk [8]. It

---

[*] Corresponding author.
E-mail addresses: rene.petervari@fhr.fraunhofer.de (R. Petervari), sebastian.karl@dlr.de (S. Karl), alexander.wagner@dlr.de (A. Wagner), peter.knott@fhr.fraunhofer.de (P. Knott).

https://doi.org/10.1016/j.ast.2026.111682
Received 18 August 2025; Received in revised form 21 November 2025; Accepted 9 January 2026

Nomenclature

parameter	description
A	range-Doppler map; [-]
$A_G, \ldots, D_G$	Gupta's correlation for $\bar{\Omega}_{ei}^{(1,1)}$; [-]
$A_B, \ldots, E_B$	Bottin's correlation for $\bar{\Omega}_{ei}^{(1,1)}$; [-]
a	target scene; [-]
$\hat{a}$	matched filter response; [-]
alt	altitude; [km]
b	measured signal; [-]
B	bandwidth; [Hz]
c_0	speed of light; $[\mathrm{m\,s^{-1}}]$
E	receive signal; [V]
E_i	incident electrical field; $[\mathrm{V\,m^{-1}}]$
E_s	scattered electrical field; $[\mathrm{V\,m^{-1}}]$
e	electron charge; [C]
f	radar frequency; [Hz]
f_C	(electron) collision frequency; [Hz]
f_D	Doppler frequency; [Hz]
f_P	(electron) plasma frequency; [Hz]
$\mathcal{F}$	Fourier transform; [-]
H	transfer function (spectrum); [m]
h	specific enthalpy; $[\mathrm{MJ\,kg^{-1}}]$
I	number of integrated slow time samples; [-]
k_B	Boltzmann constant; $[\mathrm{J\,K^{-1}}]$
L	characteristic length; [m]
L_f	flow length; [m]
m_e	electron mass; [kg]
m_s	sphere mass; [kg]
$n(s)$	number density of species s; $[\mathrm{m^{-3}}]$
Ma	Mach number; [-]
N	complex noise; [-]
Re_m	unit Reynolds number; $[\mathrm{m^{-1}}]$
r	distance to the radar; [m]
r_s	sphere radius; [m]
p	static pressure; [Pa]
s	particle species; [-]
t	time; [second]
t_f	fasttime (sampling time); [second]
t_s	slow time (waveform starting time); [second]
T	temperature; [K]
u	velocity; $[\mathrm{m\,s^{-1}}]$
$\bar{u}_e$	average electron velocity; $[\mathrm{m\,s^{-1}}]$
u_R	relative velocity w.r.t. radar; $[\mathrm{m\,s^{-1}}]$
w	waveform; [-]
Y	mass fraction; [-]
x, y, z	spatial coordinates; [m]
ϵ_0	electric field constant; $[\mathrm{A\,s\,V^{-1}\,m}]$
ϵ_r	relative permittivity; [-]
ρ	density; $[\mathrm{g\,m^{-3}}]$
$\bar{\Omega}_{ei}^{(1,1)}$	(electron) collision cross-section
λ	integration variable; [-]
λ_D	Debye length; [meter]
φ	phase; [-]
θ, ϕ	spherical coordinates; [degree]
τ	pulse duration; [second]
∞	(as index) freestream property; [-]
0	(as index) stagnation point property; [-]

requires a coherent approach of dedicated experiments and simulations to separate the impact of different models and to prove their validity or develop better ones.

In the context of ballistic missile defense and radio black out during atmospheric re-entry, microwave plasma dispersion has already been studied intensively in the 1960s and 1970s. Also ground and flight tests were conducted [6,9–11]. First indications for the importance of the wake for the radar cross-section were found in the early days of the space race, e.g. "[...t]he very large cross-section of the turbulent wake, and the large cross-section of the orthogonally polarized return[...]" [12]. Back then, however, the prediction capabilities were severely restricted by the limitation to empirical and analytical methods. A review from 1965 on hypersonic wake studies [13] lists a number complications that prevented significant progress. Among them were the absence of analytical models for turbulence and the wake flow itself, whether the chemical reaction rates differ in laminar and turbulent flow, the transition to turbulence and a model for the influence of the body shape on the structure of the wake turbulence. A few years later the research interest decayed without the problems being solved [14]. Afterwards, plasma effects were mostly investigated numerically validating against the former experiments [15,16].

Today, high performance CFD solvers are able to address some of the issues mentioned above [17,18], but topics like the transition to turbulence, hypersonic turbulence and the prediction of electron number densities still remain challenges [3,8]. Regarding the investigation of electromagnetic properties of hypersonic wakes, [19] write in their introduction, that besides theirs there are only two other relevant articles focusing on the electromagnetic signature of a hypersonic wakes by means of modern high fidelity computational approaches [20,21]. Here only the first addresses microwave scatter while the latter considers emission, leaving only [19] and [20]. Both articles, however, only consider static wakes and ignore the time-varying character of a turbulent wake flow. Time variance and Doppler signatures were considered in [22–24]. The latter [24] also shows experimental data from a ballistic range experiment.

But, despite these efforts, there is still considerable uncertainty in the prediction and understanding of plasma effects on radar signatures. To improve, a new initiative has been started to measure respective data in ground test facilities [3]. In a first series of experiments, radar returns near the stagnation point plasma of a sphere were measured in a hypersonic shock tunnel at enthalpies up to 8 MJ kg^{-1} and stagnation point temperatures up to 5000 K. Initially, the measurements agreed well with the numerical predictions obtained by combined CFD-CEM simulations [3]. In the light of new data with higher precision, however, quite significant discrepancies appeared that suggest considerable modeling uncertainties [25]. Besides that, the chemical reactions responsible for the formation of plasma were found to be very sensitive to temperature and are fostered overproportionately at high temperatures. For 8 MJ kg^{-1} CFD predicts only overdense, reflective plasma for the radar band from 3 GHz to 15 GHz near the stagnation point of the 15 cm sphere confirmed by measurements [3,25]. But for 10 MJ kg^{-1} and above an extension of the effects also into the wake is expected.

Therefore, in continuation of this approach this article presents new radar data for model validation with emphasis on broadside and wake signature. To increase the chance of measuring plasma in the wake the size of the sphere is reduced (to 8 cm) and so is the path length from the stagnation point to the wake that is subject to recombination and decay. CFD simulations predict that the reduction of the sphere radius still guarantees sufficient plasma production. Along with measurements of the radio transmission blackout, it provides monostatic radar range profiles and Doppler signatures of a plasma carrying turbulent hypersonic wake measured at high enthalpy conditions ($\geq$10 MJ kg^{-1}) in DLR's piston-driven HEG shock tunnel [26]. The study is complemented by combined numerical CFD-CEM simulations.

2. Theory

2.1. Electromagnetic plasma model

As the electromagnetic plasma model has been considered in detail in earlier contributions [3,27] it is only considered briefly here. In the microwave spectrum, relevant for radar scatter, plasma can be modeled as a lossy, dielectric medium [5, p.136]. Its permittivity ϵ_r is determined by the plasma and collision frequency, f_P and f_C, and the used microwave frequency f

$$\epsilon_r = 1 - \frac{f_P^2}{f^2\left(1 - j\frac{f_C}{2\pi f}\right)}. \tag{1}$$

The relevant electron plasma frequency is defined as

$$f_P = \frac{1}{2\pi}\sqrt{\frac{n(e^-)e^2}{\epsilon_0 m_e}}, \tag{2}$$

where $n(e^-)$ and ϵ_0 denote the electron number density and the electric field constant while e and m_e stand for the charge and mass of an electron. For the respective collision frequency a model incorporating collisional cross-sections $\bar{\Omega}_{ei}^{(1,1)}$ is used

$$f_C = \sum_{s=1}^{S} n(s)\bar{u}_e \pi \bar{\Omega}_{ei}^{(1,1)}. \tag{3}$$

It collects all collisions with particles of the S species included. The other two major parameters are the average thermal velocity of the electrons $\bar{u}_e$ and the number density of species s. Two popular methods to determine collision cross-sections have been provided by Gupta [28] and Bottin [29]. Gupta's formulation is (in $\mathring{A}^2$)

$$\pi\bar{\Omega}_{ei,Gupta}^{(1,1)} = e^{D_G} T^{A_G(\ln T)^2 + B_G \ln T + C_G}, \tag{4}$$

with A_G, B_G, C_G and D_G tabulated in Gupta et al. [28]. Bottin's alternative distinguished between charged-neutral or neutral-neutral collisions and charged-charged collisions. For the first case (charged-neutral/neutral-neutral) it states (in $\mathring{A}^2$)

$$\pi\bar{\Omega}_{ei,Bottin}^{(1,1)} = e^{[[[A_B \cdot \ln(T) + B_B]\ln(T) + C_B]\ln(T) + D_B]} \tag{5}$$

and for the latter (charged-charged) it states (in m^2)

$$\pi\bar{\Omega}_{ei,Bottin}^{(1,1)} = \frac{\pi\lambda_D^2}{T^{*2}} e^{[[[[A_B \cdot \ln(T^*) + B_B]\ln(T^*) + C_B]\ln(T^*) + D_B]\ln(T^*) + E_B]}, \tag{6}$$

$$T^* = \frac{\lambda_D}{2b_0}, \quad \lambda_D = \sqrt{\frac{\epsilon_0 k_B T}{2n(e^-)e^2}}, \quad b_0 = \frac{e^2}{8\pi\epsilon_0 k_B T}.$$

with A_B, B_B, C_B, D_B and E_B tabulated in Bottin [29]. Besides these there are a range of approaches to calculate the collision frequency and to date there is no broad agreement. The approach stated in (4), however, seems promising as it is a standard method to predict two other collision dominated processes - viscosity and diffusion - for aerothermodynamic applications [28]. It has been adopted recently also by other researchers in this field like [19,30,31]. New research indicates significant uncertainty about the collision and plasma frequency [25].

2.2. Radar basics

Radar (radio detection and ranging) is primarily a technique to measure distances over the air based on time-of-flight measurements of electromagnetic pulses. A radar system transmits a pulse and receives its scatter from the illuminated space via antennas that turn current into waves and vice versa. If receive and transmit antennas are collocated this system is called monostatic and the distance r (range) follows directly from the measured time-of-flight t_f

$$r = \frac{c_0 t_f}{2}, \tag{7}$$

when assuming a constant speed of light along the propagation path. The time-of-flight is also called fasttime to differentiate it from the time stamp of each distance measurement, which is called slowtime t_s. Another feature of radar measurements is their constant range resolution δr. It can be controlled by the B, i.e. the frequency span, of the system [32, p.63]

$$\delta r = \frac{c_0}{2B}. \tag{8}$$

2.3. Radar signal processing

Since this paper makes extensive use of radar signal processing, some central relations are reviewed here briefly. Radar primarily measures distances, i.e. ranges. The range resolution depends directly on the bandwidth of the transmitted signal - the waveform w. The received signal b is thus the convolution of the transmit waveform with the scene a. A deconvolution $\hat{a}$ would hence produce a range profile. The mathematical optimal way to do so is the optimal or Matched Filter (MF) and it results in the cross-correlation of the received signal with the transmit waveform [33, p.280]

$$b(t_f) = a(t_f) * w(t_f) \tag{9}$$

$$\hat{a}(t_f) = \int_{-\infty}^{+\infty} b(\lambda) w(\lambda - t_f) \mathrm{d}\lambda \tag{10}$$

$$= \mathcal{F}^{-1}\left(\mathcal{F}(b(t_f)) \cdot \mathcal{F}(w(t_f))^*\right), \tag{11}$$

where the $\mathcal{F}$ denotes the Fourier transform. The factor $\frac{c_0}{2}$ transforms the fasttime into range r.

Besides range, radars are often also capable of measuring Doppler frequency shifts and thus relative velocities with respect to the radar antenna. For monostatic radar, i.e. transmitter and receiver at the same position, the classical Doppler frequency shift f_D induced by relative motion at speed u_R for frequency f is given by [33, p.105]

$$f_D = -\frac{2u_R}{c_0} f. \tag{12}$$

From a set of range profiles $A(r, t_s)$ the Doppler shift can be simply obtained via another Fourier transform across the slowtime domain t_s, i.e. the time associated with each waveform

$$A(r, f_D) = \mathcal{F}\left(A(r, t_s)|_r\right). \tag{13}$$

The result is known as range-Doppler map. With (12) the range-Doppler map can be also interpreted as a range-velocity map $A(r, f_D) \approx A(r, u_R)$. For more details see e.g. [32, p.44, p.134].

Another important feature of radar data is that it is usually considered complex. It has an amplitude, i.e. the square root of the RCS, and a phase angle φ

$$\hat{a}(r, t_s) = \sqrt{\mathrm{RCS}(r, t_s)}\exp\left(j\varphi(r, t_s)\right) + N(r, t_s) \tag{14}$$

$$\text{with} \quad RCS := \lim_{r\to\infty} 4\pi r^2 \frac{|E_s|^2}{|E_i|^2} \tag{15}$$

with noise N. The RCS is hence the range independent farfield limit of the scattered field amplitude E_s normalized to the amplitude of the incident field E_i. To suppress the noise and improve detection, often multiple range profiles are averaged. However, there are multiple ways of averaging. Two important ones are the coherent and the incoherent average. The incoherent average is defined as

$$\langle \hat{a}(r) \rangle_{\text{incoh.}} = \frac{1}{I}\sum_{i=1}^{I} \left|\hat{a}(r, t_{s,i})\right|, \tag{16}$$

while the coherent average is

$$\langle \hat{a}(r) \rangle_{\text{coh.}} = \frac{1}{I}\left|\sum_{i=1}^{I} \hat{a}(r, t_{s,i})\right| \tag{17}$$

and $\langle \hat{a}(r) \rangle_{\text{coh.}} =< \hat{a}(r) >_{\text{incoh.}}$ is only true if the phase is time independent $\varphi(r, t_s) = \varphi(r)$. For the noise contribution, however, this is never true. Also, the coherent white noise average is zero, while the incoherent average is non-zero as determined by the Rayleigh distribution. The coherent average is hence advantageous for noise suppression if the phase is stable and it is hence often used in radar systems to extend the detection range. If the phase is unstable, coherent average deteriorates and can cause significantly decreased detection ranges.

3. Experiment

3.1. The high enthalpy shock tunnel göttingen (HEG)

The experiments of this study were conducted in the High Enthalpy Shock Tunnel Göttingen (HEG) located at the DLR site in Göttingen. The unique capability of HEG is the duplication of hypersonic flight conditions, not only in terms of Mach and Reynolds number, but also in static and total temperature including the high-temperature gas dynamic effects such as plasma generation in stagnation regions. HEG was originally designed for high-enthalpy test conditions to investigate the influence of high-temperature effects such as chemical and thermal relaxation on the aerothermodynamics of entry or re-entry vehicles. To meet the demand of current hypersonic research interests its test capabilities were extended to $2\,\mathrm{km\,s^{-1}}$ at altitudes ranging from sea level to 15 km ($\approx 2\,\mathrm{MJ\,kg^{-1}}$) and $6\,\mathrm{km\,s^{-1}}$ at 20 km to 30 km altitude ($\approx 23\,\mathrm{MJ\,kg^{-1}}$). Detailed information on HEG is provided in the given reference by DLR [26].

3.2. The multi-application software defined radar system (MaSoDeRa)

In its standard configuration, which has already been applied in the wind tunnel campaigns at the Institute of Saint-Louis [3,25], FHR's Multi-application Software Defined Radar (MaSoDeRa) system features a 3 to 15 GHz Linear Frequency Modulation (LFM) waveform in a high Pulse Repetition Frequency (PRF) mode at 250 kHz with direct sampling at $50\,\mathrm{GS\,s^{-1}}$. In the absence of plasma this results in a range resolution of 1.25 cm measured radially from two collocated transmit and receive antenna pair. Although this produces large data streams and the size of the buffer memory limits the observation time to 10 ms at maximum, with a maximum of 3 ms test time under the given conditions, it is still sufficient. A thorough treatment of the calibration in the environment of a wind tunnel test section and additional information on the MaSoDeRa system can be also found in Petervari et al. [3]. Additionally, for this campaign a range-Doppler processing was implemented and calibrated to enable additional evaluation (Fig. 1).

3.3. Setup

For this study an 8 cm diameter sphere made of Polyoxymethylene (POM) was suspended with nylon threads into the center of the HEG test section just behind the supersonic nozzle in the anticipated test volume (see Fig. 2). As in the previous studies [3,25] with POM ($\epsilon_r([3\,\mathrm{GHz}; 15\,\mathrm{GHz}]) = (2.99 \pm 0.03) + j(0.10 \pm 0.01)$ from FHR's internal database) a dielectric material was chosen again as it reduces the reflection at the sphere and maximizes the measured change evoked by reflective plasma. Likewise it decreases the mass for the suspension. The final choice of POM was made due to availability and due to ϵ_r (2.1 (PTFE), 2.33 (PA)) and weight being comparable to [3,25]. The sphere size was reduced to shorten the path length of the flow from the plasma source in the stagnation point area and thus also reduces the accompanied recombination and decay. Additionally, higher flow enthalpies ($9.8\,\mathrm{MJ\,kg^{-1}}$ to $11.9\,\mathrm{MJ\,kg^{-1}}$) with stagnation point temperatures between 5900 K and 6800 K were used, which foster the production of plasma and lead to higher electron densities than previously. In total, these measures increase the chances of measuring reflective plasma in the wake. During the test time in the range of a millisecond, hypersonic flow conditions are established in the test volume behind the nozzle. As mentioned, two of HEG's high enthalpy conditions were used: H9.8R2.2 and H11.9R1.5 [26]. Average flow conditions are collected in Table 1.

The scene was observed with FHR's MaSoDeRa system through the optical accesses (4) in the test section. A transmit and a receive antenna were placed side by side on one side to maintain monostatic operation, while a second receive antenna was placed on the other side of the wind tunnel to observe the transmission through the flow (cf. Fig. 2). Before each experiment, the sphere was suspended into the anticipated test volume. When the flow arrived, the threads dissolved and the sphere was practically in free flight experiencing significant acceleration. To calculate the acceleration of the sphere, the CFD surface pressure p was integrated across the sphere's surface to obtain the net force:

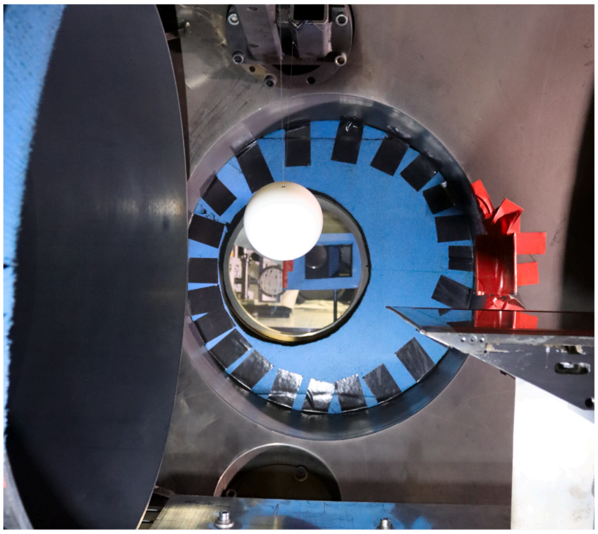

Fig. 1. The flat plate model underneath the suspended sphere model toghether with antennas in the background.

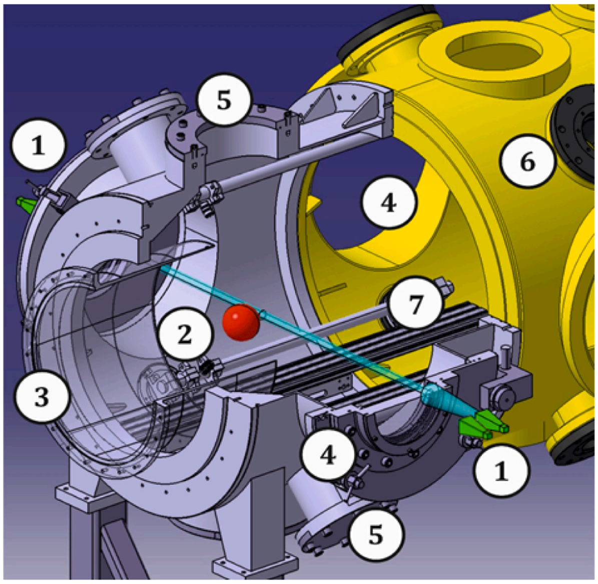

Fig. 2. A 3D visualization of the test setup with annotations: (1) radar antennas, (2) sphere model, (3) wind tunnel nozzle, (4) access door with windows, (5) additional access, (6) test section continuation, (7) rail positioning system.

$$\frac{\mathrm{d}^2 x}{\mathrm{d}t^2} = \frac{1}{m_s} \int_0^{2\pi} \int_0^{\pi} \underbrace{(p(\theta)\vec{r}_s \cdot \vec{x})}_{=p(\theta)\cos(\theta)} \underbrace{r_s^2 \sin(\theta)\mathrm{d}\theta\mathrm{d}\phi}_{surface\ element}. \tag{18}$$

For the two conditions we get

$$2335\,\mathrm{m\,s^{-2}} \quad @ \quad H = 9.8\,\mathrm{MJ\,kg^{-1}}, \tag{19}$$

$$2028\,\mathrm{m\,s^{-2}} \quad @ \quad H = 11.9\,\mathrm{MJ\,kg^{-1}}. \tag{20}$$

At the end of the test time ($\approx 3\,\mathrm{ms}$) the sphere $m_s = 378\,\mathrm{kg}$) has travelled less than one millimeter (0.47 mm @ $H = 9.8\,\mathrm{MJ\,kg^{-1}}$ and 0.41 mm @ $H = 11.9\,\mathrm{MJ\,kg^{-1}}$). Within the test time, it hence practically remains at rest inside the test volume with controlled flow conditions as the high

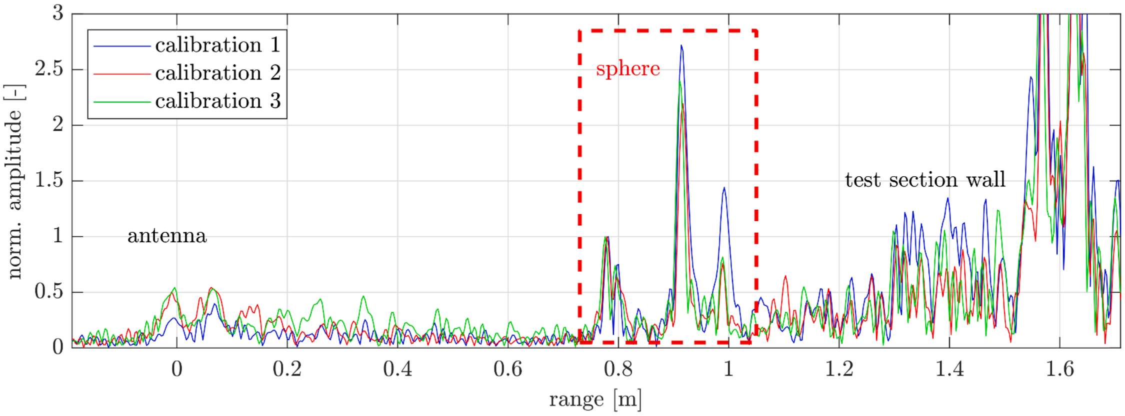

Fig. 3. Backscatter range profiles to localize the sphere (Frequency range: 3 GHz to 15 GHz).

Table 1
The nominal flow conditions of the applied HEG test conditions. Taken from [26].

condition	H9.8R2.2	H11.9R1.5
p_0 [MPa]	44.1	37.6
T_0 [K]	5932	6818
h_0 [MJ kg^{-1}]	9.8	11.9
Ma_∞ [-]	6.2	6.1
$alt(p_\infty)$ [km]	18	19
$alt(\rho_\infty)$ [km]	28	30
Re_m [m$^{-1}\cdot10^6$]	2.2	1.5
p_∞ [Pa]	7460	6761
T_∞ [K]	1084	1333
ρ_∞ [g m^{-3}]	23.5	16.9
u_∞ [m s^{-1}]	4036	4426
$Y(N_2)\|_{nozzle\ exit}$	0.7398	0.7419
$Y(O_2)\|_{nozzle\ exit}$	0.1852	0.1639
$Y(NO)\|_{nozzle\ exit}$	0.0583	0.0539
$Y(N)\|_{nozzle\ exit}$	0.0000	0.0000
$Y(O)\|_{nozzle\ exit}$	0.0167	0.0404

Table 2
The test matrix.

shot	condition	p_0 [MPa]	T_0 [K]	model
1	H11.9R1.5	40.6	6812	sphere
2	H9.8R2.2	48.4	5861	sphere

speed footage also confirms. As complication, during the experiments a heavy flat plate was also in the test section and could not be removed within the short time frame of this campaign. However, since the sharp edges prevent strong plasma generation, no strong interference is expected. Furthermore, the high range resolution of the MaSoDeRa system allows to separate the return of the flat plate and the sphere to some extent. The conducted experiments are listed in Table 2).

3.4. Calibration

Target localization and background correction. Although central system features have been validated in [3], each setup needs individual calibration. As known from prior campaigns, the backscatter signal from plasma is expected to be small compared to the background from the metallic test section. To localize the sphere in the range profiles, the background without the sphere was measured first. Then the sphere was suspended into its testing position and a second measurement was acquired. In lack of a dedicated suspension mechanism the position of the sphere varied between the tests causing variation in the measured signal amplitudes and subtraction deficiencies (see Fig. 3).

Target signature. Besides some left-overs of the antenna coupling peak used as 0 m reference, the sphere (0.77 m) and its shadow on the other side of the test section (> 1.5 m) are clearly visible (Fig. 3). The distance between the antenna and the sphere was approximately 0.8 m and the measured range profiles reflect that. Also, the POM sphere consists of two major scatterers because the material is semi-transparent for microwave radiation—a first, smaller reflection peak at the front (0.77 m) and a large peak caused by internal reflection at its back (0.91 m). The third peak is probably caused by multi-path effects since separate measurements in an anechoic chamber do not show it (cf. Fig. 10).

Calibration. As this was the first experiment of this kind in HEG, we were cautious with the transmit power to avoid signal saturation and system damage. The finally realized transmit power, however, was not recorded. And, since the team relied on offline calibration after the experiments, it was difficult to retrieve quantitative transfer functions. To work around this issue, a transfer function $H(f)$ was calculated from the measured signatures $E^i_{meas}(f)$ of a set of three metallic spheres with diameters of 40 mm, 60 mm, and 95 mm

$$H(f) = \frac{1}{3}\sum_{i=1}^{3}\frac{E^i_{theory}(f)}{E^i_{meas}(f)r_i^2}, \tag{21}$$

where $E^i_{theory}(f)$ and r_i denote the analytical solution and the respective distance of the sphere to the antenna. It is assumed that this transfer function correctly captures the relative phase and amplitude relations in the spectrum. Applied to the measured data, it corrects the relative phase and amplitude contributions and thus effectively focuses the range profile. To correct for the remaining absolute amplitude ambiguity, the prominent second peak was set to the value measured independently in the anechoic chamber.

4. Aerodynamic simulation

The CFD simulations in this study were done with the DLR TAU Code [34] which is a second order finite-volume solver for the Navier-Stokes equations. Stability and accuracy in the solution, taking into account the strong discontinuities in the flow field, was achieved by using the AUSMDV upwind-solver for inviscid fluxes and 2nd order MUSCL gradient reconstruction [34]. Boundary layers are assumed to be laminar and a constant wall temperature of 300 K was set at the solid boundaries. The solution was obtained in a 2D-axisymmetric domain. The flow is treated to be a 11-species mixture of thermally perfect gases in chemical non-equilibrium (N_2, O_2, NO, N, O, their monovalent ions and free electrons). Hence, a separate continuity equation for each species is solved. The source terms in these equations are computed using the law of mass action with the 20-step Gupta reaction mechanism [28]. The equilibrium constants are directly obtained from the thermodynamic properties of

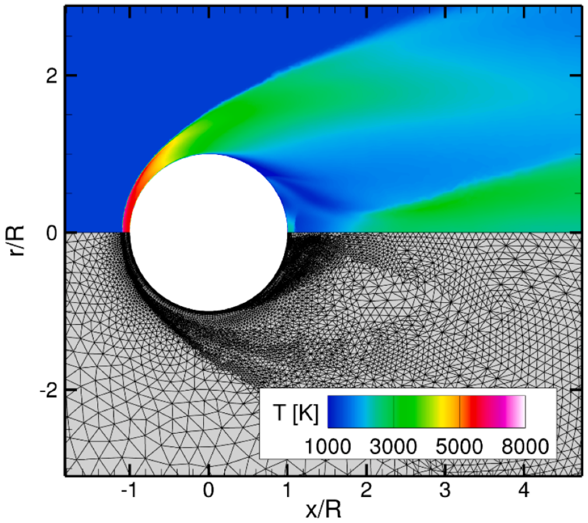

Fig. 4. Example solution of the flow around the sphere for the H11.9R1.5 free stream conditions.

the participating species. Thermodynamic properties of the individual species are calculated from partition functions applying full coupling of the rotational, vibrational and electronic excitation of the molecules [29]. The transport coefficients are evaluated from binary collision integrals using the Yos-approximation of the Chapman-Enskog expansion which neglects off-diagonal terms [29]. An example solution for the H11.9R1.5 case is shown in Fig. 4. The top part of the figure is the temperature field in the vicinity of the sphere, the bottom part shows the solution-adapted computational grid with about 26,000 control volumes.

5. Electromagnetic simulation

Based on the aerodynamic simulations, the backward and forward microwave scatter of the sphere and its wake was calculated by means of CST's Finite Difference Time Domain (FDTD) solver [35], as before in Petervari et al. [3]. The plasma and collision frequency distributions were calculated according to Eqs. (2) and (3) from the prior CFD solution described in Section 4 and imported into CST. Following the analysis in Petervari et al. [27], the background permittivity was neglected. Three cases were simulated:

1. POM sphere in a vacuum box
2. POM sphere inside a H9.8R2.2 plasma flow field
3. POM sphere inside a H11.9R1.5 plasma flow field.

The mesh features $x \times y \times z = 504 \times 317 \times 317 = 50,227,568$ cells with a size between 0.9 mm and 1.3 mm. The frequency range was set from 3 GHz to 15 GHz. For the highest frequency (15 GHz) this gives more than 15 samples per wave length - a value which has been found sufficient in the first campaign [3]. Similarly, Perfectly Matched Layers (PML) and background cells were included to minimize interaction with the boundaries. From the obtained scattered fields the backscatter Radar Cross-Section (RCS) and dummyTXdummy– the respective range profiles were derived.

6. Electron density estimation

As stated above, the objective of this work is to provide experimental reference data to mature the confidence in CFD-CEM simulations for the prediction of radar microwave scatter at plasma shrouded hypersonic vehicles. Radar relies on microwave scatter and microwave scatter at plasma interfaces is determined by the dispersion relation (1).

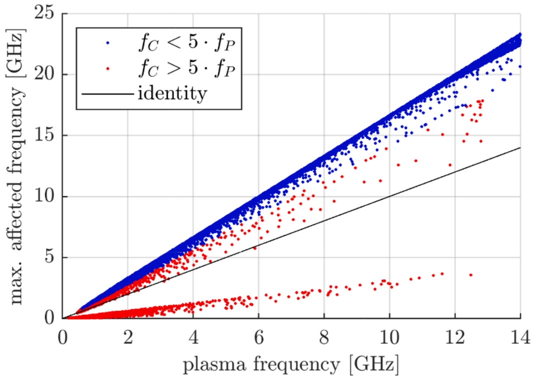

Fig. 5. The maximum affected frequency for all CFD cells from the cases H11.9R1.5 and H9.8R2.2 combined.

The respective refractive index follows from the local plasma and collision frequencies f_P and f_C which remain often unvalidated as they are not measured directly. Only the cut-off frequency associated with a change from reflective to transparent plasma is observed directly. To obtain an estimate of the actual plasma frequency based on the cut-off frequency, the present CFD data is evaluated with respect to the maximum frequency the predicted plasma can affect. The evaluation is based on the refractive index in each CFD cell. It is calculated from (1)–(3). The maximum affected frequency is estimated by the largest microwave frequency that produces a refractive index less than 0.8 and greater than 1.2. Significant deviations like these should still produce measurable reflections. Beyond, the reflections should decay and cause the cut-off. The maximum affected frequency is hence used as an estimate for the observed cut-off. Its relation with the simulated plasma frequency is given in Fig. 5.

For the present CFD data, the graph reveals that if collisions are not excessive ($f_C < 5 f_P$) the maximum affected frequency does not exceed twice the plasma frequency. Whether a plasma interface produces a reflection or not depends on the local gradient and the interface orientation with respect to the incoming microwaves. General conclusions are hence difficult. But, if a reflection exists and the plasma is not collision dominated, there are no strong effects expected far beyond the maximum affected frequency and it will eventually form a cut-off that is actually observable. If this cut-off frequency can be estimated by the maximum affected frequency that is approximately twice the plasma frequency, a rough estimate of the plasma frequency based on the measured cut-off would be

$$f_{P,\text{est}} \approx \frac{f_{\text{cut-off}}}{2} \text{if} f_P > 5 f_C. \qquad (22)$$

To find out where this requirement of non-collision dominated plasma is fulfilled, Fig. 6 shows the collision dominated areas in the flow field. Apparently, for the present test conditions these areas are only located close to the shock and do not reach zones with higher electron densities. The approximation is hence applicable to scatter from the core flow, where most of the plasma effects are expected.

7. Experimental results

The measured radar data for the conducted tests is given below. Forward and backscatter are considered separately.

7.1. Backscatter

7.1.1. Range profiles

To study the general properties of the measured backscatter range profiles, the respective time series of shots 1 and 2 are shown in Fig. 9. A sketch to help interpretation is given in Fig. 7. To enhance the small

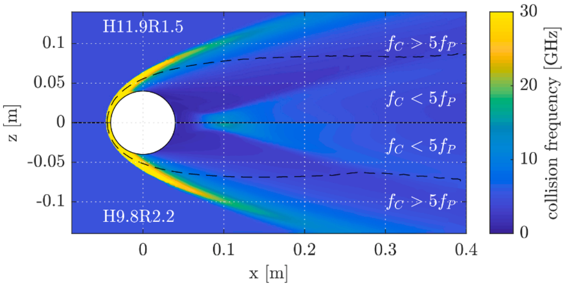

Fig. 6. Regions with collision dominated plasma lie outside the coreflow around the sphere.

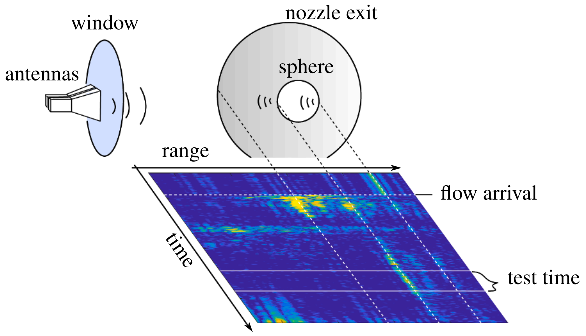

Fig. 7. Interpretation of radar range profiles.

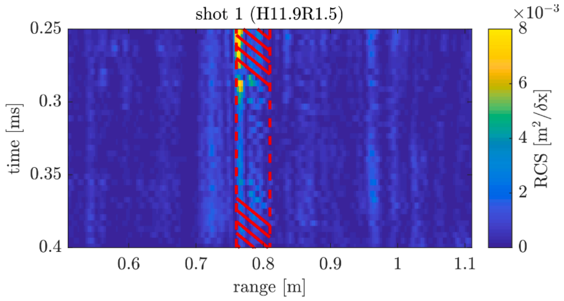

Fig. 8. Example for ropelike structures observed in shot 1. Here, strongest effects are encountered between 0.27 ms and 0.37 ms. Where not visible their orientation is sketched in red. (For interpretation of the references to colour in this figure legend, the reader is referred to the web version of this article.)

changes visually, background subtraction was applied. The range profiles acquired after the test, when the sphere is gone, were used as background estimate. Although this is not ideal, because the nozzle moves during operation a few cm downstream, it was found appropriate in most cases. Furthermore, from the calibration (Section 3.4) we know that the returns of the sphere and its plasma sheath are expected in the range between 0.7 m and 1.0 m. And indeed, at 0.77 m between 0.3 ms and 0.5 ms after flow arrival there is a significant change in the signal. The first reflection peak at 0.77 m is enhanced and the secondary peak associated with the back of the sphere disappears, i.e. the pronounced 0.91 m peak.

Ropelike Structures. Additionally, ropelike structures were observed (Fig. 8) that indicate motion of scatterers towards larger distances. These structures seem to originate primarily from the first peak at 0.77 m. To further investigate this phenomenon, a Doppler analysis follows in the section below.

Disturbances. Another insight from the range profiles is that there is a significant change near the antenna between 0 m and 0.5 m. Camera footage has shown that with the advent of the flow, a turbulent stagnation area emerges in the window hole of the test section (cf. Fig. 2 (4)). As plasma emerges in stagnation regions it is likely that plasma also emerges near the windows and causes the strong changes that are observed in the measurements. A second observation that supports this interpretation, is that there is another scatterer at 0.5 m that emerges together with the arrival of the flow and moves towards the antenna/window region at 0 m. By linearly extrapolating the motion, its arrival falls together with the generation of the disturbances between 0 m and 0.5 m. Its dynamics indicate that this scatterer can be identified with the initial shock front that enters the test section. It is a possible explanation why the flow near the window seems to be initially (between 0.0 ms and 0.5 ms) transparent. At that time the initial shock wave has not arrived at the window and hence leaves no dense plasma in the field of view. Since the off-axis flow towards the windows should be less intense than the core flow jet coming out of the nozzle, the expected plasma at the window should also be less dense. By adjusting the frequency range, these contributions could thus be reduced. And indeed, a restriction of the used frequency range to the band between 8 GHz and 15 GHz suppresses the initial disturbances significantly, making the plasma in the window hole transparent.

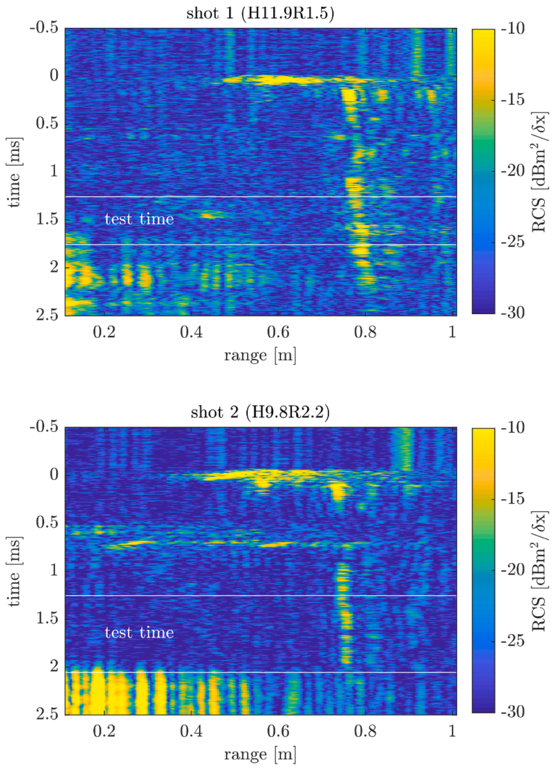

Fig. 9. The measured backscatter for each experiment in the frequency range 8 GHz to 15 GHz. The data is normalized to the back reflection peak at 0.91 m and multiplied with its value measured in the anechoic chamber. The white lines indicate the test time.

After narrowing the bandwidth down to the 8 GHz and 15 GHz band, the data shows clear indication for the presence of plasma effects around the sphere (see Figs. 9 and 7). During the test time the flow obscures the 0.91 m peak, while it enhances the 0.77 m one. However, although this peak has a rather stable position its phase is not stable. As a consequence

$$\langle \hat{a}(r)\rangle_{\text{incoh.}} \gg \langle \hat{a}(r)\rangle_{\text{coh.}}, \tag{23}$$

suggesting incoherence which potentially mitigates coherent integration and could thus deteriorate detection (Section 2.3). Since the Doppler processing is sensitive with respect to phase variation, the analysis in Section 7.1.2 also addresses this issue.

Simulations. At first, three CFD-CEM simulations have been conducted for comparison. The results for the coherently and incoherently

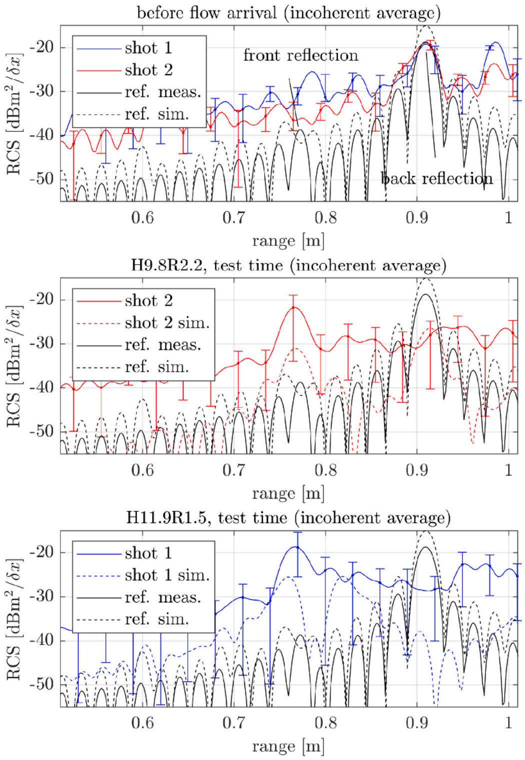

Fig. 10. Comparison of measured (incoherent average, Eq. (16)) and simulated backscatter range profiles in the frequency range 8 GHz to 15 GHz before and during the test time.

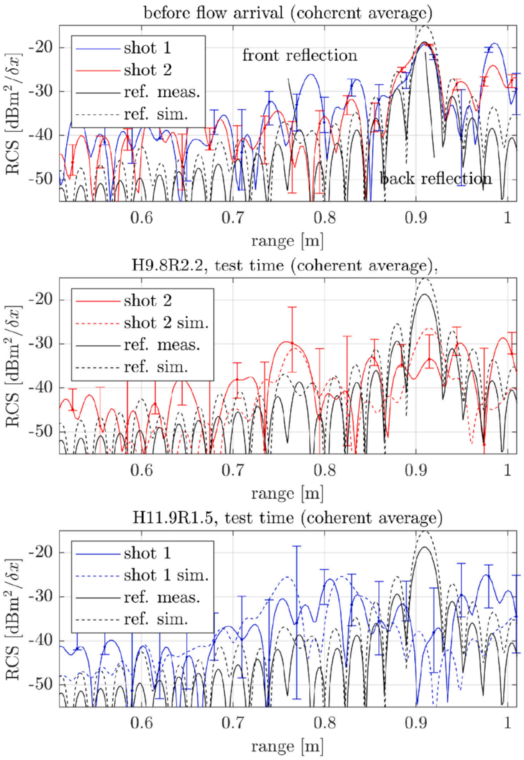

Fig. 11. Comparison of measured (coherent average, Eq. (17)) and simulated backscatter range profiles in the frequency range 8 GHz to 15 GHz before and during the test time.

averaged backscatter RCS are shown in Figs. 10 and 11, respectively, with direct comparison against the amplitude average from Fig. 9.

A first observation is that the simulation successfully predicts the attenuation of the 0.91 m back reflection peak and the enhancement of the 0.77 m front reflection peak. Secondly, it also predicts the larger reflection of shot 1 (H11.9R1.5) compared to shot 2 (H9.8R2.2). This is true for both the coherent and incoherent RCS average. For the incoherent RCS, however, despite a good qualitative agreement the absolute predictions deviate by 6 dB to 8 dB from the measurements. Astonishingly, simulation and experiment agree better if coherent integration is used (Fig. 11). This is a clear indication of incoherence as will be further investigated in the Doppler section below. Despite the good match, this ignores the presence of the practically always much stronger reflection with almost random phase at the 0.77 m peak. Also, it is possible that the coherent average accounts more for the smooth and static part of the plasma sheath and thus fits better.

A possible reason for this difference might be that in the simulation turbulent structures are neglected and all surfaces are practically smooth. For fusion plasmas, however, [36] has shown that turbulent structures can change electromagnetic backscatter significantly. Also [12] mentions a large contribution coming from turbulent flow in the hypersonic wake that carries plasma. Since the resolution of small turbulence scales is computationally exceptionally expensive, it has been neglected here, although it may be necessary to accurately predict the RCS. Another reason may be that the predicted plasma state does not match the experimental case. Spurious elements like iron that are produced in significant numbers during the operation of the tunnel or small portions of ablated surface material of the model could affect the chemical reactions and cause this bias as shown in Psarras et al. [37]. Similarly, an underestimation of the number of freestream electrons that were produced by the high temperatures in the nozzle reservoir and did not recombine until they reached the model could change the reflection properties. A dedicated freestream characterization with respect to chemical species could help here to improve the model. However, these issues need further treatment but are beyond the scope of this contribution.

Sensitvity study. Assuming modeling deficiencies regarding the plasma and collision frequency, their distributions were multiplied by a set of factors ($f'_p = \{1,2,3\} \cdot f_p$, $f'_c = \{0.1, 0.3, 1, 3\} \cdot f_c$). The traces of the front and rear peaks are shown in Fig. 12. Changes in the collision frequency would require large deviations beyond a factor of 10, i.e less than 0.1 and it appears that it probably already is in saturation and a further decay would not yield larger amplitudes. Instead, an increase of the plasma frequency by a factor between 1 and 2 seems to improve the situation in the front. But still, this again assumes a smooth plasma sheath which it probably is not. Hence, to improve the predictions, the roughness of the plasma sheath should certainly be taken into account.

7.1.2. *Doppler signatures*

To further investigate the encountered ropelike structures (Fig. 8), range-Doppler maps were derived from the time series of range profiles and averaged across the test time with a sliding 300 µs window. The results for the 8 GHz to 15 GHz band are shown in Fig. 13. Due to the large bandwidth spanned in these experiments, the Doppler is subject to multiple frequencies and underlies some spread. From (12) follows that

$$u_R = -\frac{f_{D,meas}c_0}{2f} \tag{24}$$

$$\Rightarrow \quad u_R \in \left[-\frac{f_{D,meas}c_0}{2\cdot 8\,\mathrm{GHz}}, -\frac{f_{D,meas}c_0}{2\cdot 15\,\mathrm{GHz}}\right] \tag{25}$$

$$\approx (1 \pm 0.3)u_R \quad (@10.4\,\mathrm{GHz}). \tag{26}$$

The velocity displayed in Fig. 13 thus shows a velocity error of 30 %. The precision can be increased by reducing the frequency band at the cost of range resolution. The current setting appears to be a good compromise.

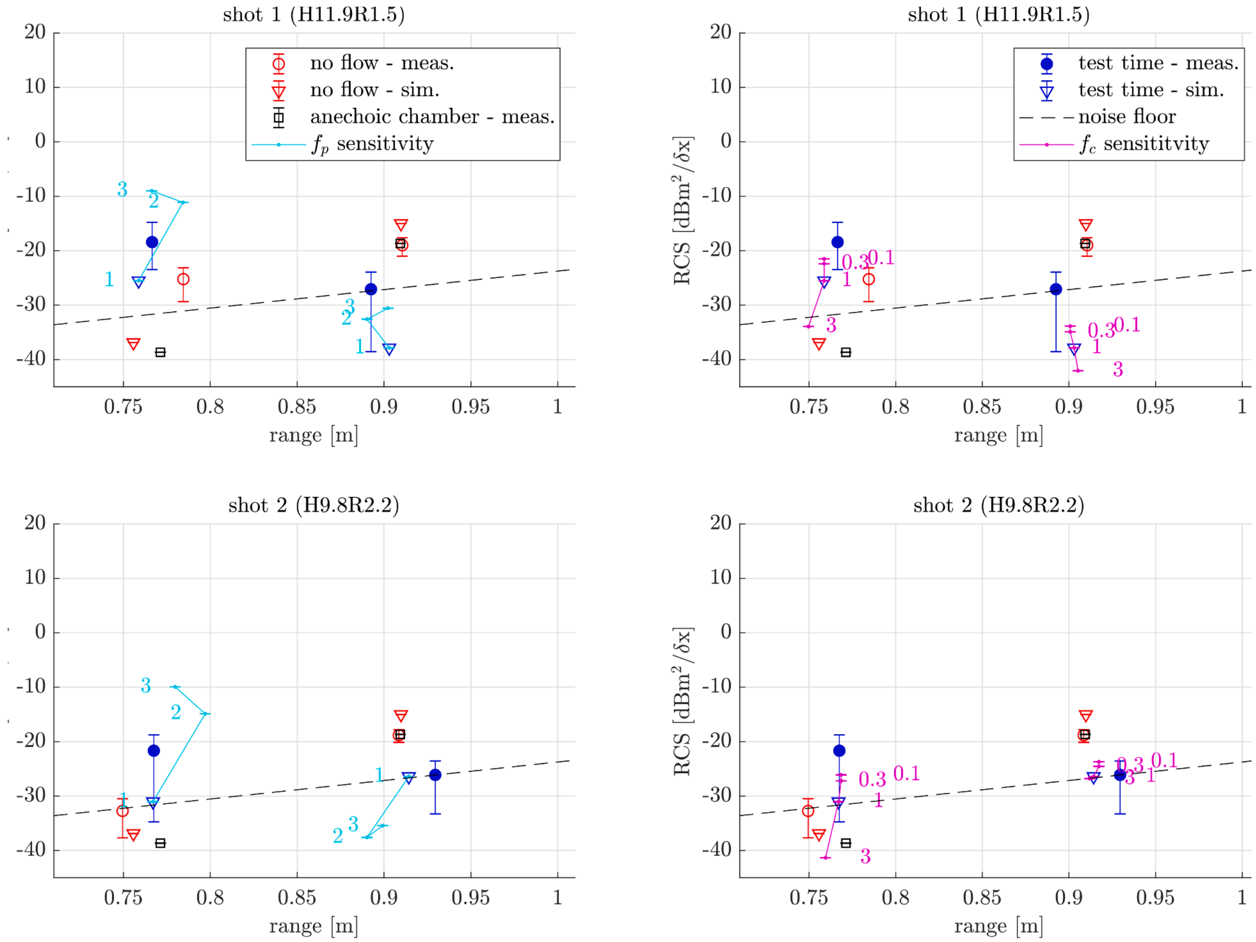

Fig. 12. The effect of the variation of the plasma and collision frequency on the front peak and rear peak values in the text referred 0.77 m and 0.91 m, respectively. The legend is split across the four subplots for better readability. The sensitivity line graphs display the results of the plasma and collision frequency distributions multiplied by the factors next to it.

A very prominent Doppler signal appears near the front peak at 0.77 m, where the ropelike structures emerge and incoherence was observed. The reason is apparently a wide Doppler spread. It shows a departing, accelerating motion which is stationary over time and with values up to more than $1000\,\mathrm{m\,s^{-1}}$. Calculations (18) have shown that the spheres are practically at rest throughout the test time and thus cannot be the source of this frequency shift. Instead, such high velocities evoke the association of scatterers transported with the flow. This association is also supported by the ropelike structures in Fig. 8 where the lines detaching from the 0.77 m scatterer invoke the idea of scatterers moving forward in time to larger ranges, i.e. departing from the radar.

Origin. To identify the origin of these scatterers within the flow field the range-velocity radar measurement $A_{meas}(r, u_R)$ and the simulated velocity flow field $u_{R,CFD}(x, y)$ are combined with the range $r(x, y)$ to produce an estimate for the volume that causes the reflection

$$A(x, y) = A_{meas}(r(x, y), u_{R,CFD}(x, y)). \tag{27}$$

The results for experiment 1 and 2 are shown in Fig. 14 together with the CFD plasma frequency and the areas with strong refractive indices (center). For convenience, all areas in front of the shock and with $|u_R| < 100\,\mathrm{m\,s^{-1}}$ were set to zero. The images show an averaged reflection between −0.07 m and −0.01 m for both cases, although the $11.9\,\mathrm{MJ\,kg^{-1}}$ case has higher amplitudes and a slightly larger extent than the $9.8\,\mathrm{MJ\,kg^{-1}}$ case. This agrees well with the simulated plasma frequency distribution that also predicts higher electron densities and a larger extent for the $11.9\,\mathrm{MJ\,kg^{-1}}$ case. The earliest reflection viewed from the antenna at $(x, y) = (0.05, -0.81)$ also agrees well with the predicted increase of electron density at −0.070 m ($11.9\,\mathrm{MJ\,kg^{-1}}$) and −0.065 m ($9.8\,\mathrm{MJ\,kg^{-1}}$), respectively.

Wake characteristics. So far, it has been implicitly assumed that by the start of the test time the wake has already started. For reflected shock tunnels like HEG a value between 50 to 100 flow length ($L_f = \frac{tu_\infty}{L}$) is given in the literature Park et al. [38], Lin et al. [39]. In our case this means

$$L_f(H = 9.8\,\mathrm{MJ\,kg^{-1}}) = \frac{1\,\mathrm{ms} \cdot 4036\,\mathrm{m\,s^{-1}}}{0.08\,\mathrm{m}} \approx 51 \tag{28}$$

$$L_f(H = 11.9\,\mathrm{MJ\,kg^{-1}}) = \frac{1\,\mathrm{ms} \cdot 4426\,\mathrm{m\,s^{-1}}}{0.08\,\mathrm{m}} \approx 55, \tag{29}$$

which is within the margin, but only at the very left end of it. Therefore, it is important to highlight that the conditions do not guarantee a fully evolved wake, but certainly show instationary behavior behind the sphere that is also visible in the camera footage and probably responsible for the measured incoherence.

Constituents. The scatterers that follow the flow could be both metallic particles or plasma carrying turbulent vortices (eddies). To find out which hypothesis is more persuasive, their reflective properties are compiled briefly.

If metallic dust particles originating from the operation of the tunnel were seeding the wind tunnel flow, they would accumulate in denser regions as friction grows with density and thus also the resident time

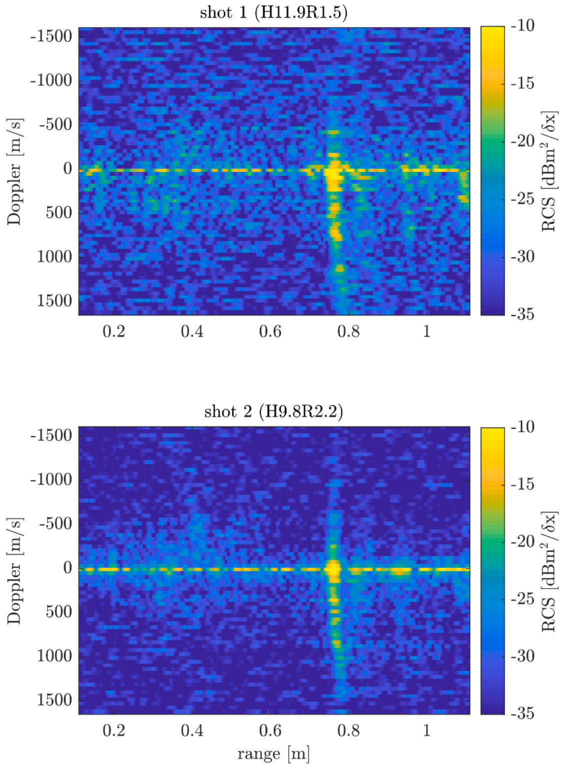

Fig. 13. The averaged Doppler map during the test time in the 8 GHz to 15 GHz band. The Doppler axis was calculated for 10.4 GHz.

in a certain area. This would increase the reflectivity of this area with respect to vacuum. Higher density would thus cause larger reflections. However, it is rather questionable that there is sufficient seeding during the test time as optical footage is usually rather clear. Also, for sufficient seeding, no strong frequency dependencies would be expected, other than observed below.

If the scatterers were instead caused by plasma, they should obey the dispersion relation. A cut-off would be a clear indication for the presence of plasma. Furthermore, as plasma emerges from the flow, it should reflect properties obtained from CFD. Hence, to analyze the measured Doppler signals, the CFD flow field was investigated with respect to its microwave impact quantified by the real part of the refractive index. Fig. 14 (center) shows the real part of the refractive index calculated from (1) in the cross-section of the flow field. For convenience, all areas with velocities $< 500\,\mathrm{m\,s^{-1}}$ and refractive indices within $[0.9, 1.1]$ were ignored. Assuming that the measured signal is caused by plasma and the radar system at $(x, y) = (0.1\,\mathrm{m}, -0.7\,\mathrm{m})$, leads to two major regions where significant effects are expected: just behind the first broadside scatterer $(0\,\mathrm{m}, -0.04\,\mathrm{m})$ around $(0.05\,\mathrm{m}, -0.02\,\mathrm{m})$ and behind the second scatterer, i.e. the back reflection, $(0\,\mathrm{m}, 0.04\,\mathrm{m})$ around $(0\,\mathrm{m}, 0.05\,\mathrm{m})$. And indeed, the measurements show a small Doppler signal beyond the 0.91 m peak in experiment 1. For shot 2 there are only traces. But the simulations in Fig. 14 (center) also show that the secondary area is smaller for the H9.8R2.2 case, and hence shot 2 with lower enthalpy which could indicate less reflection.

Characteristics. To improve the accuracy of the Doppler measurement and to create a frequency resolution, the integration band was reduced from 8 GHz to 15 GHz to a 2 GHz sliding window. To maintain 2-D-plotting the resulting range Doppler maps were averaged across range Σ_D (across $0.6\,\mathrm{m} < R < 0.9\,\mathrm{m}$) and Doppler Σ_R (across $f_D > 1500\,\mathrm{m\,s^{-1}}$), respectively. The results are shown in Figs. 15 and 16. First, the Doppler average Σ_R shows that the main peak amplitude varies with the flow condition and correlates with the change in enthalpy. A behavior that is reflected by the electron density predicted in the CFD solution and causing the refractive index variation in Fig. 14 (center). Secondly, the range average Σ_D shows a clear frequency dependence of the Doppler velocity with a cut-off with no effects above a certain frequency and strong effects below. This is a clear indication for the presence of plasma since (1) shows that if $f_P > f$ and $f_C = 0$ there is a surface with $\epsilon_r = 0$ that denies waves from propagating and causes reflection. Furthermore, this cut-off depends on the velocity and the condition.

Electron density. Now, to derive an electron density estimate from the measured data, (22) is applied. It requires that the main reflection originates from areas with $f_C < 5 f_P$. Fig. 14 shows that the reflection is mainly caused by the dense plasma in the wake and Fig. 6 shows that this requirement is fulfilled here. Hence, the observed cut-off frequencies in Fig. 16 are used to estimate the electron density. Fig. 17 compares the estimated plasma frequencies and hence electron densities with the collection of CFD cells with respective electron densities. The measured and predicted upper limits for the electron density show good agreement. The plot also provides an explanation for the saturation of the frequency band. There are many CFD cells which have sufficient electron densities and hence plasma frequencies to cause sensible disturbances in the measured frequency band between 8 GHz and 15 GHz.

To clarify, this is an integral measurement of the overall cut-off frequency in the illuminated area within the range between 0.6 m to 0.9 m. The electron density can be measured directly from the estimated cut-off frequency. Here, frequency resolution is key, however, it depends on the integration time, i.e. the range. Therefore, the integrated range is maximized and the spatial resolution is lost. From the velocity measurement some localization could be derived, but without the range information it is highly ambiguous and hence omitted here.

7.2. Transmission

Microwave transmission through a plasma at frequencies near its plasma frequency typically causes blackout phenomena. A comprehensive review on radio blackout is given in Gillman et al. [40]. The radio blackout and plasma sheath backscatter share the same physics as they both rely on microwave propagation in plasma. To analyze the direct transmission path through the plasma wake of the sphere, the matched filter response can be used as it provides accurate time-of-arrival measurements (Fig. 18). The first peak in the signal before the flow arrives is related to the direct line-of-sight path as this is the shortest one and produces the least time difference. All other multi-path components arrive later as their path length is longer. With the advent of the flow, this first direct line-of-sight peak is both delayed and attenuated. Until 1 ms after flow arrival and before the test time, the transmission channel (i.e. the first peak) shows a complete blackout. The blackout duration seems to increase with enthalpy. Only later, when the flow decays again (≈ 4 ms after flow arrival), the direct transmission begins to restore and shift back to the undisturbed case.

Attenuation and delay are well-known features of microwave propagation in plasma. The group velocity, relevant for the waveform propagation and hence the MF measurements, is reduced in plasma [5, p.137] and the collision frequency makes complex refractive index areas accessible (Eq. (1)) causing attenuation on transmission. So the observation agrees well with the presence of dense plasma along the line-of-sight path between the opposing transmit and receive antenna pair. Furthermore, the data shows that the signal distortion increases with enthalpy. It is likely that this behavior is caused by the increased electron production due to larger stagnation areas with higher temperatures at higher enthalpies.

To retrieve more information from the transmission channel and make comparisons with simulations, it is necessary to associate measured features with the flow around the target body. However, because of the rather wide beam that covers the whole target body with its flow,

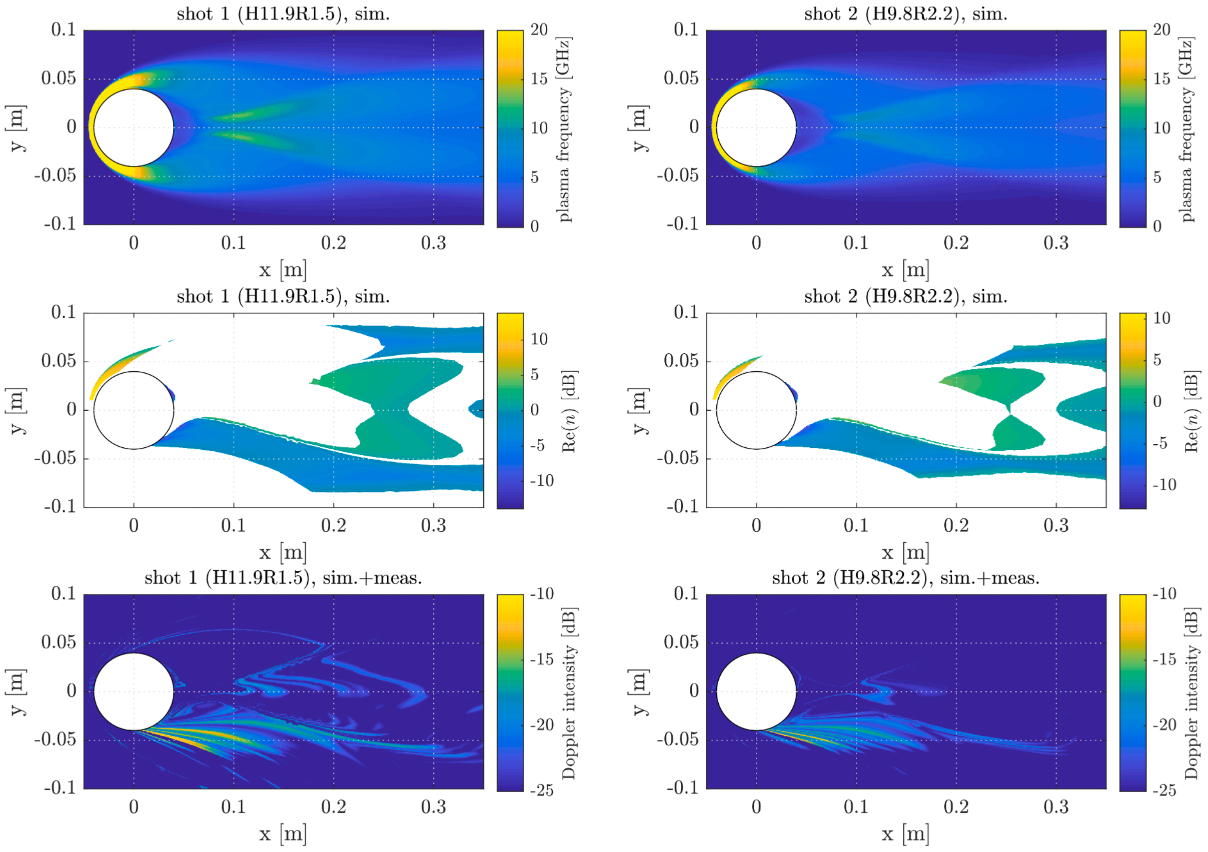

Fig. 14. The simulated plasma frequency distrbution (top). The real part of the refractive index with relative velocities larger than $500\,\mathrm{m\,s^{-1}}$ and refractive index values beyond $[0.9, 1.1]$ (center). The measured reflection area $A(x, y)$ for experiments 1 and 2 for 8 GHz to 15 GHz compared to the respective electron density simulations (bottom).

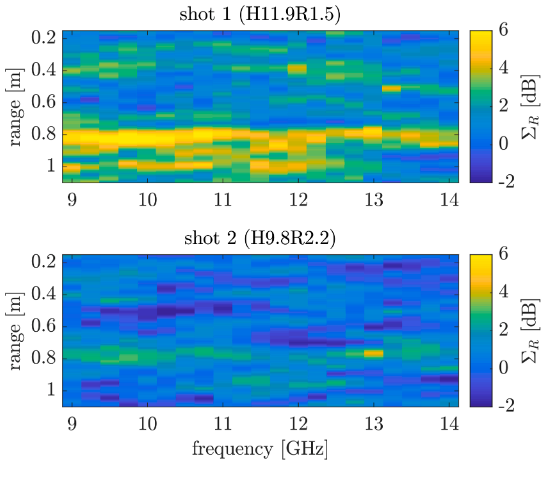

Fig. 15. The Doppler content integrated across $f_D > 1500\,\mathrm{m\,s^{-1}}$ as a function of frequency and range during the test time normalized to the noise level.

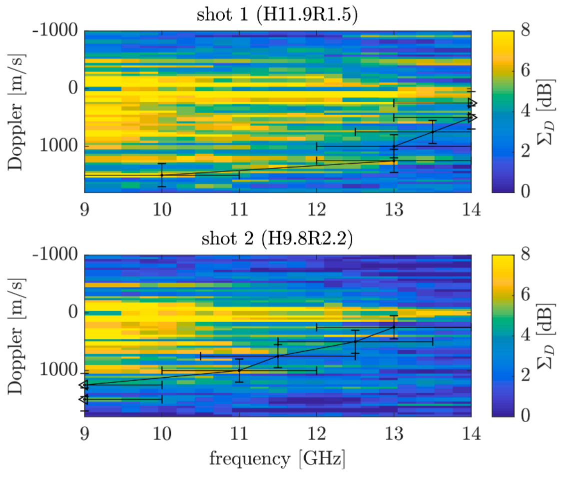

Fig. 16. The Doppler content integrated across $0.6\,\mathrm{m} < R < 0.9\,\mathrm{m}$ as a function of frequency and Doppler during the test time normalized to the noise level.

the first transmission peak integrates all these contributions. A later separation appears difficult since detailed knowledge about essential contributions like turbulence and wake structure that would enable to trace the rays through the body flow is unavailable. Furthermore, even if present, this information would be very sensitive to any kind of disturbance and, eventually, it must be questioned whether this qualifies for a mature test case that was the aim of this study. Further investigations on the transmission channel are hence abandoned.

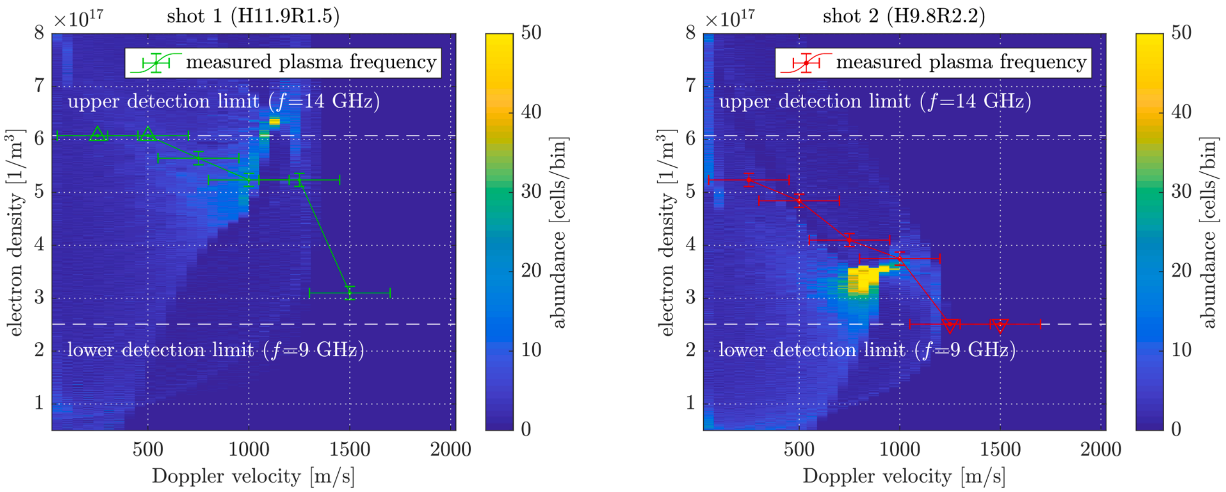

Fig. 17. A comparison of the measured and simulated plasma frequency. Saturation is indicated by triangles in the respective color.

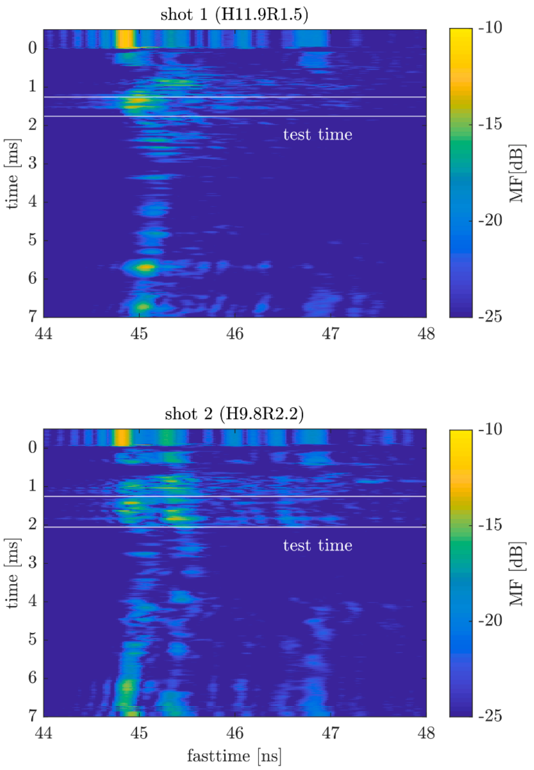

Fig. 18. The MF response obtained from the 8 GHz to 15 GHz band with focus on the test time interval. The test time indicated in white.

8. Conclusion

To address the issue of missing reference data to validate CFD-CEM simulations for radar-plasma signatures, a series of high enthalpy shock tunnel tests have been conducted in DLR's High Enthalpy Shock Tunnel in Göttingen (HEG). Radar forward scatter and backscatter of a hypersonic plasma sheath around an 8 cm POM sphere were measured at an aspect angle of 90° broadside. Several features were found.

1. Under the given flow conditions with enthalpies between 9.8 MJ kg^{-1} and 11.9 MJ kg^{-1}, a strong backscatter peak forms at the front of the plasma shroud covering all following target peaks.
2. This broadside scattering center shows large, but incoherent reflection. The incoherent component is 8 dB to 10 dB larger than the coherent one. It is probably caused by the turbulent character of the flow behind the sphere's equator that also affects the plasma shroud. This results in a wide Doppler spread of this scattering center and potentially affects coherent integration as Eq. (23) indicates. It is likely that this effect will also occur in flight since wake turbulence is present in flight and plasma in the turbulent wake has been reported as source of strong cross-polar returns [12].
3. While the CFD-CEM simulation could reproduce the influence of enthalpy on the coherent backscatter quite well, this was not possible for the large incoherence. The conducted RANS simulation did not resolve the turbulent flow and thus cannot account for turbulence. Resolving turbulence thus has high potential to improve the current results.
4. Analyzing the measured Doppler content revealed a possibility to measure the electron density associated with a certain velocity and compare it with the simulation. This comparison showed good agreement in terms of order of magnitudes supporting CFD with its aerodynamic models. To emphasize, the geometry and the physics of microwave propagation imply that the obtained electron density measurements are not point-like and can only be associated with a certain range and a coarse Doppler velocity estimate. In order to improve the validation of CFD simulations of electron density distributions more localized electron density measurement techniques like Langmuir probes [41,42] and dedicated spectroscopy methods [43] are preferred.
5. While such detailed conclusions were not obtained from the transmission channel, strong plasma-driven blackout phenomena were observed during the start-up phase of the flow leading to distortion and attenuation. Another indication for the presence of plasma. However, it was difficult to associate this information with predictable flow variables and no further insights were found.

After all, this study underlines what prior studies have shown [25,37]: the improvement of the simulation of radar-plasma signatures still requires some work. Calculated plasma and collision frequencies exhibit considerable uncertainties [25] and realistic effects like turbulence and ablation [37] add further complexity. These effects are usually not fully modeled in current CFD-CEM simulations like ours. Large Eddy Simulations (LES) or Direct Numerical Simulations (DNS) could help to resolve turbulence and including chemical ablation models would provide more realistic electron densities in ablation dominated flows. Besides this, it will be essential to clarify the definition of the collision frequency and to resolve the ambiguity of models [25]. A practical way ahead is the continuation of joint simulation and experimentation gradually improving the methods with experimental evidence and enabling reliable predictions of radar signatures of plasma shrouded hypersonic vehicles. Given the considerable uncertainty about the interplay of all included models, it makes sense to eliminate complications systematically first and gradually increase complexity. First, a good choice might be to change the test facility to a ballistic range where the test gas is at rest, not ionized or excited simplifying the determination of free-stream conditions. Second, the experiments should be accompanied by alternative measurement techniques for electron density like Langmuir probes [41,42] or spectroscopy methods [43] and maybe at cases where independent models exist, e.g. for light strips [44–47]. This way parts of the model can be tested independently without always including the whole chain of CFD and CEM models. Third, a better localization of the measurement is helpful. In this context microwave reflectometers must be mentioned as they have been used on the RAM C-II vehicle [48]. They can be embedded into models and detect the reflectivity of the plasma layer just above it.

CRediT authorship contribution statement

René Petervari: Writing – review & editing, Writing – original draft, Visualization, Validation, Supervision, Software, Resources, Project administration, Methodology, Investigation, Formal analysis, Data curation, Conceptualization; **Sebastian Karl:** Writing – original draft, Visualization, Software; **Alexander Wagner:** Resources, Investigation, Conceptualization; **Peter Knott:** Writing – review & editing.

Data availability

Data will be made available on request.

Declaration of generative AI and AI-assisted technologies in the writing process

During the preparation of this work the authors used FhGenie in order to improve the language in parts of the work. After using this service, the authors reviewed and edited the content as needed and take full responsibility for the content of the publication.

Declaration of competing interest

The authors declare that they have no known competing financial interests or personal relationships that could have appeared to influence the work reported in this paper.

Acknowledgments

The authors like to thank DLR's HEG team for facilitating these measurements.

References

[1] D. Bok, J. Schell, P. Knott, Relatively moving target return emulation for high coherently processed time-bandwidth products, in: 2022 IEEE Radar Conference (RadarConf22), IEEE, 2022.
[2] M. Gunar, R. Mennella, Signature studies for a re-entry system in: The Space Congress Proceedings - 1965 (2nd) New Dimensions in Space Technology, 1965.
[3] R. Petervari, S. Weidner, A. Nekris, S. Brüggenwirth, P. Knott, The measurement of radar-plasma-signatures in a hypersonic shock tunnel: simulation and experiment, IEEE Trans. Aerosp. Electron. Syst. 59 (6) (2023) 8581–8597.
[4] J.D. Anderson, Jr, Hypersonic and High-Temperature Gas Dynamics, American Institute of Aeronautics and Astronautics, 2006.
[5] A. Piel, Plasma Physics: An Introduction to Laboratory, Space, and Fusion Plasmas, Springer, 2017.
[6] W.L. Jones, Jr., A.E. Cross, Electrostatic-Probe Measurements of Plasma Parameters for Two Reentry Flight Experiments at 25 000 Foot Per Second, Technical Report NASA-TN-D-6617, Langley Research Center, 1972.
[7] R. Grosso Ferreira, J. Vicente, F. Silva, B. Gonçalves, L. Cupido, M. Lino da Silva, Reflectometry diagnostics for atmospheric entry applications: state-of-the-art and new developments, CEAS Space J. 16 (1) (2024) 1–18.
[8] S. Karl, T. Bykerk, Sustainable space technologies-strategies toward a predictive aerothermal design of re-useable space transportation systems, Rev. Sci. Instrum. 95 (2) (2024).
[9] W.E. Blore, H.M. Musal, Millimeter radar instrumentation for studying plasma effects associated with hypersonic flight, Technical Report TR64-02J, GM Defense Research Laboratories, 1964.
[10] W.L. Darnell, Radar Cross Section and Optical Radiation from the Trailblazer IIa 9 deg Half-Angle Blunt Nose Cone During Hypersonic Reentry, Technical Report TN D-3214, Langley Research Center, 1966.
[11] D.W. Boyer, S.N. Andre, Theoretical and Experimental Studies of Microwave Interaction Effects in a Hypersonic Air Plasma, Technical Report, Cornell Aeronautical Lab., Inc., Buffalo, NY, 1972.
[12] P.A. Ingwersen, W.Z. Lemnios, Radars for ballistic missile defense research, Lincoln Lab. J. 12 (2) (2000) 245–266.
[13] P.S. Lykoudis, A Review of Hypersonic Wake Studies (RM-4493-ARPA), Technical Report, The RAND Corporation, Santa Monica, CA, USA, 1965.
[14] T.W. Johnston, Limits to plasma science, Proc. IEEE 69 (2) (1981) 149–158. https://doi.org/10.1109/PROC.1981.11947
[15] T. Lin, L. Sproul, D. Hall, J. Sontowski, Reentry plasma effects on electromagnetic wave propagation, in: 26th Plasmadynamics and Lasers Conference, 1995, p. 1942.
[16] D. Mather, J. Pasqual, J. Sillence, P. Lewis, Radio frequency (RF) blackout during hypersonic reentry, in: AIAA/CIRA 13th International Space Planes and Hypersonics Systems and Technologies Conference, 2005, p. 3443.
[17] G.V. Candler, P.K. Subbareddy, I. Nompelis, CFD methods for hypersonic flows and aerothermodynamics, Hypersonic Nonequilibr. Flows Fundam. Recent Adv. (2015) 203–237. https://doi.org/10.2514/5.9781624103292.0203.0238
[18] G.V. Candler, Rate effects in hypersonic flows, Annu. Rev. Fluid Mech. 51 (2019) 379–402.
[19] S. Esposito, A. Scarabosio, G. Vecchi, D. D'Ambrosio, Non-equilibrium plasma distribution in the wake of a slender blunted-nose cone in hypersonic flight and its effect on the radar cross section, Aerosp. Sci. Technol. 155 3 (2024) 109699.
[20] J.-W. Qian, H.-L. Zhang, M.-Y. Xia, Modelling of electromagnetic scattering by a hypersonic cone-like body in near space, Int. J. Antennas Propag. 2017 (1) (2017) 3049532.
[21] J. Tong, H. Li, B. Xu, S. Wu, L. Bai, Excitation and power spectrum analysis of electromagnetic radiation for the plasma wake of reentry vehicles, Plasma Sci. Technol. 25 (5) (2023) 055301.
[22] Y. Ding, B. Bai, H. Gao, Y. Liu, X. Li, M. Zhao, Method of detecting a target enveloped by a plasma sheath based on doppler frequency compensation, IEEE Trans. Plasma Sci. 48 (12) (2020) 4103–4111.
[23] Y. Ding, B. Bai, H. Gao, G. Niu, F. Shen, Y. Liu, X. Li, An analysis of radar detection on a plasma sheath covered reentry target, IEEE Trans. Aerosp. Electron. Syst. 57 (6) (2021) 4255–4268. https://doi.org/10.1109/TAES.2021.3090910
[24] B. Jiang, X. Yang, P. Ma, B. Chen, J. Tian, A. Shi, P. Tang, Contactless measurement of hypervelocity projectile wake velocity distribution, IEEE Access 7 (2019) 28968–28972.
[25] R. Petervari, S. Weidner, K. Psarras, F. Denis, P. Knott, Assessing the accuracy of radar-plasma signature simulations using hypersonic shock-tunnel data with variable freestream oxygen levels, Aerosp. Sci. Technol. 168 (2026) 110858. https://doi.org/https://doi.org/10.1016/j.ast.2025.110858
[26] J.M. Schramm, A. Wagner, D. Surujhlal, G.P. Camillo, The high enthalpy shock tunnel göttingen of the german aerospace center (DLR), J. Large-Scale Res. Facil. JLSRF 9 (1) (2024).
[27] R. Petervari, A. Nekris, T. Bieker, Numerical analysis of radar-plasma-signatures of asphere in a mach 10 hypersonic wind tunnel flow, in: 2021 18th European Radar Conference, 2022.
[28] R.N. Gupta, J.M. Yos, R.A. Thompson, K.-P. Lee, A review of reaction rates and thermodynamic and transport properties for an 11-species air model for chemical and thermal nonequilibrium calculations to 30000 K (1990).
[29] B. Bottin, Aerothermodynamic Model of an Inductively-coupled Plasma Wind Tunnel: Numerical and Experimental Determination of the Facility Performance, Von Karman Institute for Fluid Dynamics. (1999). https://books.google.de/books?id=2VtLHAAACAAJ
[30] Y. Takahashi, Propagation path of radio waves in nonequilibrium reentry plasma around a nanosatellite with an inflatable aeroshell, IEEE Trans. Aerosp. Electron. Syst. 58 (5) (2022) 4070–4082. https://doi.org/10.1109/TAES.2022.3158625
[31] A. Scarabosio, J.L.A. Quijano, J. Tobon, M. Righero, G. Giordanengo, D. D'Ambrosio, L. Walpot, G. Vecchi, Radiation and scattering of EM waves in large plasmas around objects in hypersonic flight, IEEE Trans. Antennas Propag. 70 (6) (2022) 4738–4751.
[32] P. Tait, Introduction to Radar Target Recognition, 18, IET, 2005.
[33] M.I. Skolnik, Introduction to Radar Systems, McGraw Hill, New York, third edition edition, 2001.
[34] N. Kroll, S. Langer, A. Schwöppe, The DLR flow solver TAU-status and recent algorithmic developments, in: 52nd Aerospace Sciences Meeting, 2014, p. 0080.
[35] D. Systémes, CST Microwave Studio, CST Studio Suite Documentation, 2023.
[36] F. Da Silva, S. Heuraux, E. Ricardo, A. Silva, T. Ribeiro, Modelling reflectometry diagnostics: finite-difference time-domain simulation of reflectometry in fusion plasmas, J. Instrum. 14 (08) (2019) C08003.
[37] K. Psarras, R. Petervari, F. Denis, T. Ecker, F. Kessel, P. Knott, Measuring the influence of ablation on hypersonic plasma trails in ISL's hyperballistic tunnel by means of radar: simulation and experiment, in: 59th 3AF International Conference on Applied Aerodynamics, 24th-26th March 2025, Strasbourg, France, 2025.
[38] G. Park, R. Hruschka, S.L. Gai, A.J. Neely, Flow establishment behind blunt bodies at hypersonic speeds in a shock tunnel, in: 28th International Congress on High-Speed Imaging and Photonics, 7126, SPIE, 2009, pp. 175–182.

[39] Y. Lin, J.J. Wallington, C.M. James, T. Bui, T.J. van den Herik, E.W.K. Chang, T.A. Hermann, Expansion tube capabilities for studying boost-glide re-entry conditions, CEAS Space J. 17 (2025) 699–720.

[40] E.D. Gillman, J.E. Foster, I.M. Blankson, Review of Leading Approaches for Mitigating Hypersonic Vehicle Communications Blackout and a Method of Ceramic Particulate Injection via Cathode Spot Arcs for Blackout Mitigation, Technical Report, 2010.

[41] M.G. Dunn, J.A. Lordi, Measurement of electron temperature and number density in shock-tunnel flows. I-Development of free-molecular Langmuir probes, AIAA J. 7 (8) (1969) 1458–1465.

[42] M.G. Dunn, J.A. Lordi, Measurement of electron temperature and number density in shock-tunnel flows. II, AIAA J. 7 (11) (1969) 2099–2104.

[43] A.P. Rao, M. Gragston, A.K. Patnaik, P.S. Hsu, M.B. Shattan, Measurement of electron density and temperature from laser-induced nitrogen plasma at elevated pressure (1–6 bar), Opt. Express 27 (23) (2019) 33779–33788. https://doi.org/10.1364/OE.27.033779

[44] G.G. Lister, S.E. Coe, GLOMAC: a one dimensional numerical model for steady state low pressure mercury-noble gas discharges, Comput. Phys. Commun. 75 (1-2) (1993) 160–184.

[45] H. Ja'afar, M.T. Ali, A.N. Dagang, I.P. Ibrahim, N.A. Halili, H.M. Zali, Reconfigurable plasma antenna array by using fluorescent tube for Wi-Fi application, Proceedings of Czech and Slovak Technical Universities 25 (2) (2016).

[46] A.N. Dagang, C.X. Lei, H. Ja'afar, Study on the effect of a variation taypes of gas pressures and coupling sleeves on the performance of monopole plasma antenna, ARPN J. Eng. Appl. Sci. 12 (23) (2017) 6649–6656.

[47] N. Roslan, A.N. Dagang, R. Umar, Adjustable antenna using plasma medium, Univ. Malays. Terengganu J. Undergrad. Res. 3 (4) (2021) 21–32.

[48] W.L. Grantham, Reentry plasma measurements using a four frequencyreflectometer, in: Symposium on the Entry PlasmaSheath and Its Effects on Space Vehicle Electromagnetic Systems (4th Plasma Sheath Symposium), October 13–15, NASA LangleyResearch Center, Hampton, Virginia, 1970.